Journal of Materials Science: Materials in Electronics (2019) 30:4069–4078
https://doi.org/10.1007/s10854-019-00694-6

Lanthanum modified BFO–BT solid solutions: a structural, electrical and magnetic study

C. Behera[1] · R. N. P. Choudhary[2] · Saroj K. Parida[1]

Received: 1 May 2018 / Accepted: 4 January 2019 / Published online: 9 January 2019

Abstract
In this paper, structural, electrical and magnetic characteristics of Lanthanum-modified multiple perovskite $BiFeO_3$–$BaTiO_3$(BFO–BT) solid solutions have been reported. Detailed structural analysis via Rietveld refinement technique using X-ray diffraction pattern provides the evolution of a mono-phase distorted perovskite structure with the concurrence of rhombohedral structure. Scanning electron micrograph of La modified BFO–BT solid solutions at ambient temperature exhibits that with varying La content in the material, more symmetric structure, high density and uniform grain distribution are obtained. The dielectric parameters are strongly depends on composition, frequency and temperature. The well defined polarization–electric field hysteresis loop of the samples at room temperature suggests that La substitution at the Bi site of the solid solutions strongly affects remnant and saturated polarization of the materials. The low lanthanum concentration in the solid solutions is able to provide a well-defined ferromagnetic characteristic with saturation magnetization (M_s) in the range of 6–9 emu/g and remnant magnetization(M_r) 1.5–2 emu/g and shows that BT substitution in BFO releases latent magnetization whereas addition of higher content of barium titanate shows an anti-ferromagnetic behaviour which has been confirmed by M-H hysteresis loop and Arrot plots. Based on the derived parameters of La modified solid solution, it is expected to fabricate a multifunctional device.

1 Introduction

Now a days, materials with diverse functional microscopic order parameters, (i.e., charge, spin, lattice and orbital) have been found more prospective for multifunctional electronic devices, including memory, sensors and spintronic devices. Though coexistence of more than one order parameters or macroscopic phenomenon (i.e., ferromagnetism, ferroelectricity and/or ferroelasticity) in a single phase material is rare [1], attempts have still been made to develop such type of materials for devices. Recent discovery of above characteristics in a mono-phase bismuth ferrite ($BiFeO_3$) has attracted a special attention of the researchers to work with it owing to its novel and excellent multiferroic characteristics well above room temperature (i.e., anti-ferromagnetic phase transition (T_N) between 347 and 397 °C, ferroelectric Curie temperature (Tc) between 807 and 877 °C) [2]. Unfortunately, some of its inherent problems (i.e., formation of impurities phases, creation of oxygen vacancies and defects, structural instabilities, leakage current, etc.,[3]) have restricted it for real device applications. During last decades, several attempts have been made to solve these problems of $BiFeO_3$ [4–6] such as by (i) introducing some suitable elements at the *Bi*/*Fe* sites, (ii) fabrication of solid solution or composites with other polar or non-polar structure and (iii) developing new processing techniques and (iv) introducing the tetragonal ferroelectric phase for the enhancement of multiferroic properties [7]. Many research work have already been reported on the enhancement of multiferroic characteristics by several experimental strategy on synthesis of single phase and its characterization. For example, partial replacement of comparable ions (Gd^{3+}, La^{3+} and Sm^{3+}) for Bi^{3+} [8–10] and/or Al^{3+}, Co^{3+} for Fe^{3+} [11] in the $BiFeO_3$ lattices, and fabrication of solid solution and/or composite of $BiFeO_3$ (BFO) with another lead based $Pb(ZrTi)O_3$, [9] $Pb(MgNb)O_3$, [13, 14] and lead-free perovskite ($BaTiO_3$) [15] ferroelectrics have provided many important results for applications. Among all the perovskites, eco-friendly $BaTiO_3$ (BT) has been found a more suitable candidate for

✉ C. Behera
cdbehera1986@gmail.com

[1] Department of Physics, National Institute of Technology, Agartala, Tripura 799046, India

[2] Department of Physics, Siksha'O'Anusandhan, Deemed to be University, Bhubaneswar 751030, India

fabrication of a solid solution with BFO because of its excellent ferroelectric properties ($T_c = 120$ °C, $P_s = 26$ μC/cm^2 and $\varepsilon_r > 1000$) [16] for device applications [17, 18]. Some studies of BFO-based binary solid solutions (BFO–BT) have shown ferromagnetism [2], though one (BFO) is anti-ferromagnetic and another one (BT) is ferroelectric at room temperature. On increasing the concentration of BT in a solid solution of these two, the rhombohedral distortion increases and the level of ferromagnetic order decreases [19]. It has also been observed that non-isovalence substitutions (i.e., Ba^{2+} at the Bi^{3+} and Ti^{4+} at the Fe^{3+} sites) lead to a complex structural change [20]. Detailed literature survey reveals that the substitution of iso-valence lanthanides (i.e., *La, Sm, Nd, Gd, Dy*, etc) [21] at the Bi^{3+} site of BFO has a number of important consequences, including change of symmetry, and property from anti-ferromagnetic to ferromagnetism. Among these lanthanides, substitution of La^{3+} at Bi^{3+} can drastically change the multiferroic characteristics of $BiFeO_3$ (thin films or bulk). It is because of integrating space regulated spin structure, minimizing the leakage current density, maximizing the ferroelectric characteristics, [22] stabilizing the crystal structure by reducing distortion, demolishing space modulated spin structure and liberating weak ferromagnetism [22, 23]. Though some works have already been carried out on the lanthanide (including La) modified BFO–BT solid solution, there are still some problems to solve some problems, such as, preparation of impurities-free BFO–BT solid solution, which have subsequently hampered to get optimum multiferroic response of bismuth ferrite [24–27]. In view of the important role of lanthanum substitution to solve the inherent problems (namely, enhancement of multiferroic properties and removal of some anomalies of the earlier reports), we have carried out the systematic work on synthesis and characterization of *La*-modified BFO–BT (BLBFT) solid solutions. In this communication, an important role of lanthanum substitution on structural, dielectric, ferroelectric and transport properties of BFO–BT solid solutions (synthesized by a cost effective solid state route) have been reported.

2 Materials and methods

The polycrystalline solid solutions of La-modified $BiFeO_3$–$BaTiO_3$ of chemical compositions $(Bi_{0.5-x}\,La_xBa_{0.5})(Fe_{0.5}Ti_{0.5})O_3$ (where $x = 0, 0.05, 0.10, 0.15, 0.20$) were synthesized using a cost effective high-temperature solid-state reaction technique by taking high-purity (> 99.9% or analytical grade) oxides or carbonate; namely bismuth oxide Bi_2O_3 (M/s Loba Chemie Co Ltd), Fe_2O_3 (iron oxide) (M/s CDH Co Ltd), barium carbonate $BaCO_3$ (M/s Loba Chemiel Co Ltd), titanium dioxide TiO_2 (M/s Loba Chemie Co Ltd) and lanthanum oxide La_2O_3 (M/s Loba Chemie Co Ltd) in a required stoichiometry. A small amount (4%) of extra Bi_2O_3 has been added to the mixture of above compounds to prepare the solid solution in order to compensate the loss of bismuth during the high-temperature processing of the materials. All the ingredients were ground thoroughly by dry (air) as well as wet (methanol) mode in an agate mortar and pestle for 2 h. The homogeneously mixed powders were calcined at the optimized temperature in the temperature range of 970–1000 °C for 6 h in a covered alumina crucible [for Lanthanum concentration $x = 0.0, 0.05, 0.10, 0.15$ and 0.20 the calcination temperature are 970, 975, 980, 990 and 1000 respectively]. The diffraction patterns and data of the calcined powders were obtained by X-ray powder diffractometer of M/s Bruker (model D8 Advance) with wavelength 1.5418 Å in a slow speed scan mode (rate of scanning = 1°/min). To validate the reliability of the experimental data with the theoretical one, Rietveld refinement method was carried out with material analysis using by diffraction (MAUD) software. Different crystal symmetries were validated with the diffraction patterns before arriving to the final structure. The pellets of a small dimension (10 mm diameter and 1–2 mm thickness) were fabricated using polyvinyl alcohol PVA (binder) mixed powders by a KBR hydraulic press at 7×10^7 kg/m^2 pressure. The sintering of the pellets of the compounds was carried out in the temperature range of 1050–1100 °C for 4 h in the alumina crucible [the sintering temperature for the Lanthanum concentration $x = 0.0$, 0.05, 0.10, 0.15 and 0.20 are 1050, 1060, 1070 and 1100 °C respectively]. For electrical measurements, highly conducting silver paste was painted on the flat and parallel surfaces of the sintered pellets, and annealed at 200 °C for 12 h. The dielectric and related parameters were measured over a wide range of frequency (50 Hz–1 MHz) and temperature by a LCR meter (model Agilent E4980A of M/s Agilent Technologies Inc.). In order to examine the ferroelectric characteristics of the materials, field dependence of polarization (P–E loops) was traced at room temperature using P–E loop tracer of M/S Marine India Co Ltd of the electrically poled (medium silicon oil, dc field of 2.5 kV/mm) samples. The magnetic moment of the samples was measured using a superconducting quantum interferometric device (SQUID) magnetometer of M/s Quantum Design at room temperature.

3 Results and discussion

3.1 Crystal phase analysis

The X-ray diffraction (XRD) patterns of $(Bi_{0.5-x}La_xBa_{0.5})(Fe_{0.5}Ti_{0.5})O_3$ (i.e., $x = 0, 0.05, 0.10, 0.15, 0.20$) are depicted in Fig. 1 with its Rietveld refinement data. As evident from the XRD patterns, the distinguished peaks are found broadly identical as regard to location and

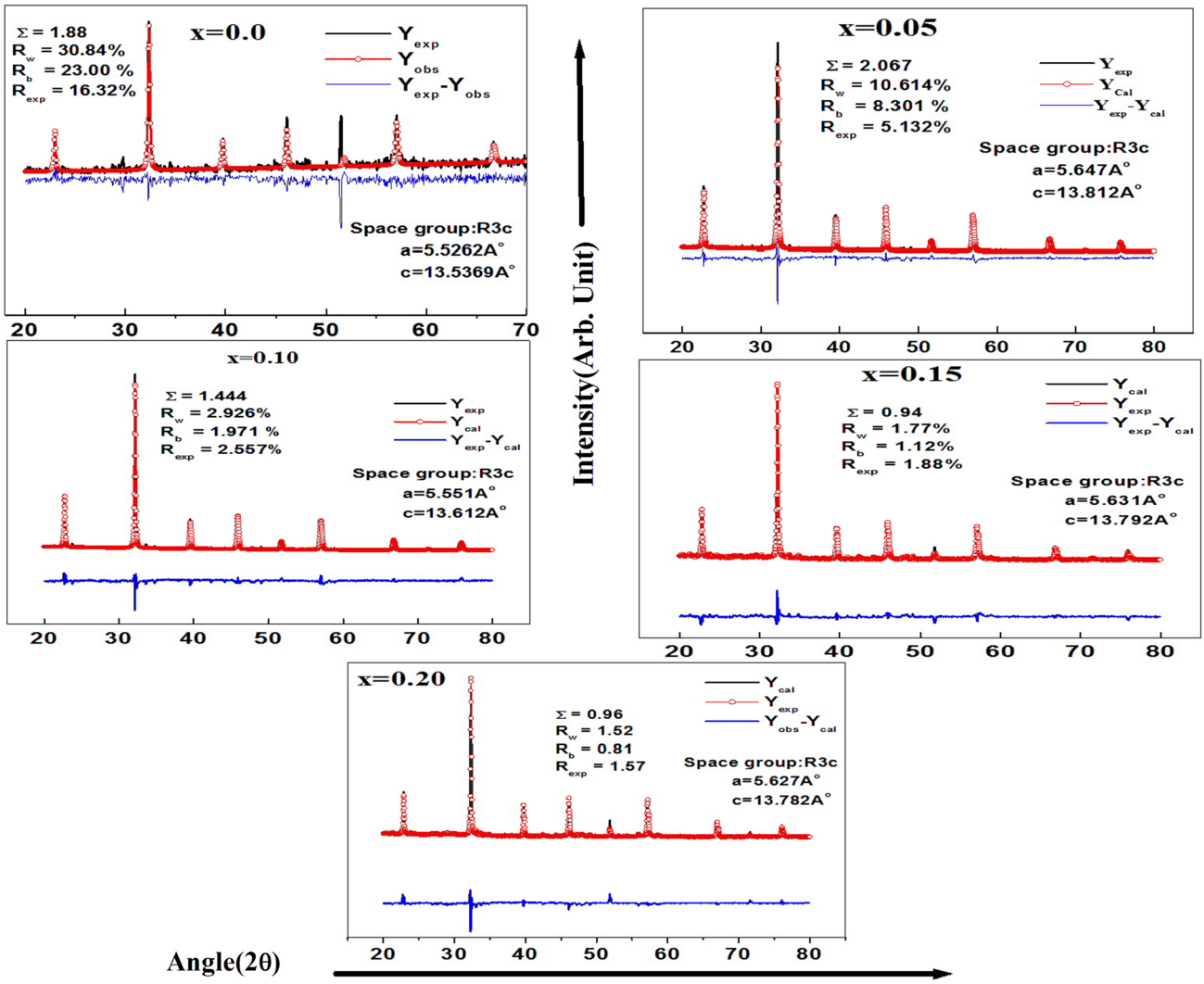

Fig. 1 Reitveld refinement of La- modified BFO–BT solid solutions

intensity with those of a perovskite structure. Thus, it can be concluded that the materials have been formed in a single-phase perovskite. BFO–BT being a rhombohederally distorted cubic perovskite, where distortion establishes by the collective rotation of an octahedral structure oriented in the (111) direction. It has been reported that the interaction of *6p* and *6 s* orbital of Bi^{3+} stimulates a vital character in inducing octahedral distortion [17]. The inclusion of Ba^{2+} (with empty p orbital) at the *Bi*-site not only reduces the motion of *Bi* ion, but also hampers the structural distortion [28]. The XRD patterns of the prepared solid solutions show the splitting of some higher angle reflection peaks which infer the formation of rhombohedral phase. On increasing lanthanum concentration, the peak position of some reflections gradually shifts towards higher *2θ* angle, and becomes nearly single-sharp peak (Fig. 1a). As these peaks correspond to cubic symmetry, it indicates the un-detectable structural evolution from rhombohedral to cubic symmetry [29]. The larger atomic radii of Ba^{2+} (1.35 Å), as compared to that of Bi^{3+} (1.03 Å), might also be responsible for peak shift. It is noted that Fe^{3+} (0.64 Å) and Ti^{4+} (0.605 Å) have almost same ionic radii [29]. The distinguished peaks of the patterns (matching with $BiFeO_3$ and/or $BaTiO_3$) were enumerated with *2θ* values of diffraction peaks using a computational package "POWD" and used to find out the phase of samples [30]. Based on the best agreement between observed (obs) and calculated (cal) value of the interplanar spacing *d* (i.e., $\sum \Delta d = d_{obs} - d_{cal} = \text{minimum}$), structural phase was scrutinized. Using a least-squares refinement sub-routine of the above software, the unit cell parameters were refined. The crystallite size (*P*) of the sample has been calculated using Scherer's formula; $P = (0.89 \times \lambda)/\beta cos\theta$, where β refers to broadening (full

width at half maxima = FWHM) of a reflection peak (*h k l*), wavelength (λ) = 1.5406 Å and θ is Bragg's angle. The average crystallite size is found to be 36, 43, 39, 37, 41 nm for the sample with x = 0, 0.05, 0.10, 0.15, 0.20 respectively. With the mixed occupancy of *La, Bi* and *Ba* at the A-site and *Fe* and *Ti* at the B-site, the peak broadening could be determined. The unsystematic displacements in 2θ of reflections may be one of the reasons for the broadening of the XRD profile. For the determination of crystal phase, lattice parameters and space group of the lanthanum modified BFO–BT solid solutions, Rietveld refinement method was found to be most suitable. Rietveld refinement were carried out using MAUD software prior to the analysis of XRD pattern of the solid solutions, first a standard sample (whose diffraction pattern is recorded with same scanning rate/step size as that of the prepared samples) was carried out to nullify the instrumental effect on the diffraction patterns. After the analysis of the standard sample, the instrumental file was saved for further analysis. Rietveld refinement of diffraction pattern of samples was carried out by introducing the previously formulated instrumental file. By using the CIF (Crystallographic Information File), the diffraction pattern of the samples was compared with that of simulated pattern through the minimization of residual or fitting parameters and all the variable structural parameters are refined by appropriating an iterative least-squares strategy. Careful comparison of the experimental diffraction patterns with the simulated one indicates that *La*-modified BFO–BT solid solutions (up to x = 0.2) is formed in a single phase (i.e., without any trace of impurities), however, a small impurity phase is found in sample without *La* (Fig. 1b). Further, structural analysis of the prepared samples was carried out with the combined CIF files of the prototype phases (i) rhombohederal $BiFeO_3$ (space group *R3c*) and (ii) cubic $BaTiO_3$. By using asymmetrical pseudo-Voigt (*pV*) function, the configuration of peaks of experimental diffraction pattern can excellently be explained, since background of each peak is fitted with a fourth order of a polynomial function. For this purpose, firstly, the background is refined; position of the peak is corrected for zero-shift error by sequential refinements, and then structural parameters are refined. The reliability or residual parameters; R_{wp} (weighted residual), R_{exp} (expected), Σ (sigma/goodness of fit) (R_{wp}/R_{exp}), show a good agreement of the fitted and simulated data with those of observed ones. However, a small degree of secondary phase is observed in the sample with no La (x = 0.0) suggesting the formation of pyrochlore phases of Bi-compounds, such as $Bi_2Fe_4O_9$, $Bi_{24}Fe_2O_{39}$, or $Bi_{25}FeO_{40}$ [31]. This observation is also evident from the analysis of scanning electron micrographs (next section). Since BT concentration in all samples is constant, the variation of La content in the sample is mainly responsible for the structural modification and stabilization. Thus, it is concluded that the lanthanum substitution in the solid solutions plays an important role in modification and stabilization of structural parameter of the BFO–BT electronic system [32, 33].

3.2 Microstructure

Figure 2 compares the scanning electron micrographs (SEM) of $(Bi_{0.5-x}\ La_xBa_{0.5})\ (Fe_{0.5}Ti_{0.5})O_3$ (x = 0, 0.05, 0.10, 0.15, 0.20). In these micrographs, it is observed that on increasing La concentration in the solid salution, the compactness (density) of well defined and uniform grain distribution in morphology increases because of the decrease in grain size and increase of lanthanum content. The substitution of La^{3+} at the Bi^{3+}-sites not only segregate grains at grain boundaries, but also stop grain growth [34]. However, a few pores inhomogeneously distributed in the sample without *La* suggest the presence of a certain degree of porosity as well as impurity in the sample (as discussed in the previous section). It is a established fact that even with a small level of defects (voids and oxygen vacancies) in microstructure drastically modifies the physical and electrical properties of the ceramic samples. A small level of oxygen vacancies (formed by the absence of Fe^{2+}), might decrease the leakage current density, having a positive effect on their electrical properties [22]. The grain distribution and size analysis has been performed with Imagej software and whose result has been added in the Fig. 2. Beside this EDAX spectrum of x = 0.0 and x = 0.20 shows that all the assigned elements have been present in the sample without any loss. As evident from the grain distribution histogram that the maximum average size of grain for x = 0.0, 0.05, 0.10,0.15,0.20 is found to be 1,0.1,0.5,0.05 and 0.025 μm respectively.

3.3 Dielectric study

The frequency dependence of relative permittivity or dielectric constant (ε_r) and tangent loss (tan δ) of $(Bi_{0.5-x}La_xBa_{0.5})(Fe_{0.5}Ti_{0.5})O_3$, (x = 0, 0.05, 0.10, 0.15, 0.20) at room temperature has been presented in Fig. 3 left panel and right panel respectively. As a normal characteristic of dielectric materials, both ε_r and tan δ parameters decrease on increasing frequency [35]. The low-frequency and high-permittivity slant on account of grain boundary impact whereas the high-frequency and low-permittivity locale demonstrates the indelible bulk impact. The relative permittivity response at low-frequency of *La*-modified BFO–BT assumes high esteems (> 1000), as the temperature increases. The mechanism of space charge polarization (supported by Maxwell–Wagner mechanism) is mainly responsible for high value of dielectric constant in the materials. In this case, the grain is seen to offer a similar low resistance and activation energy

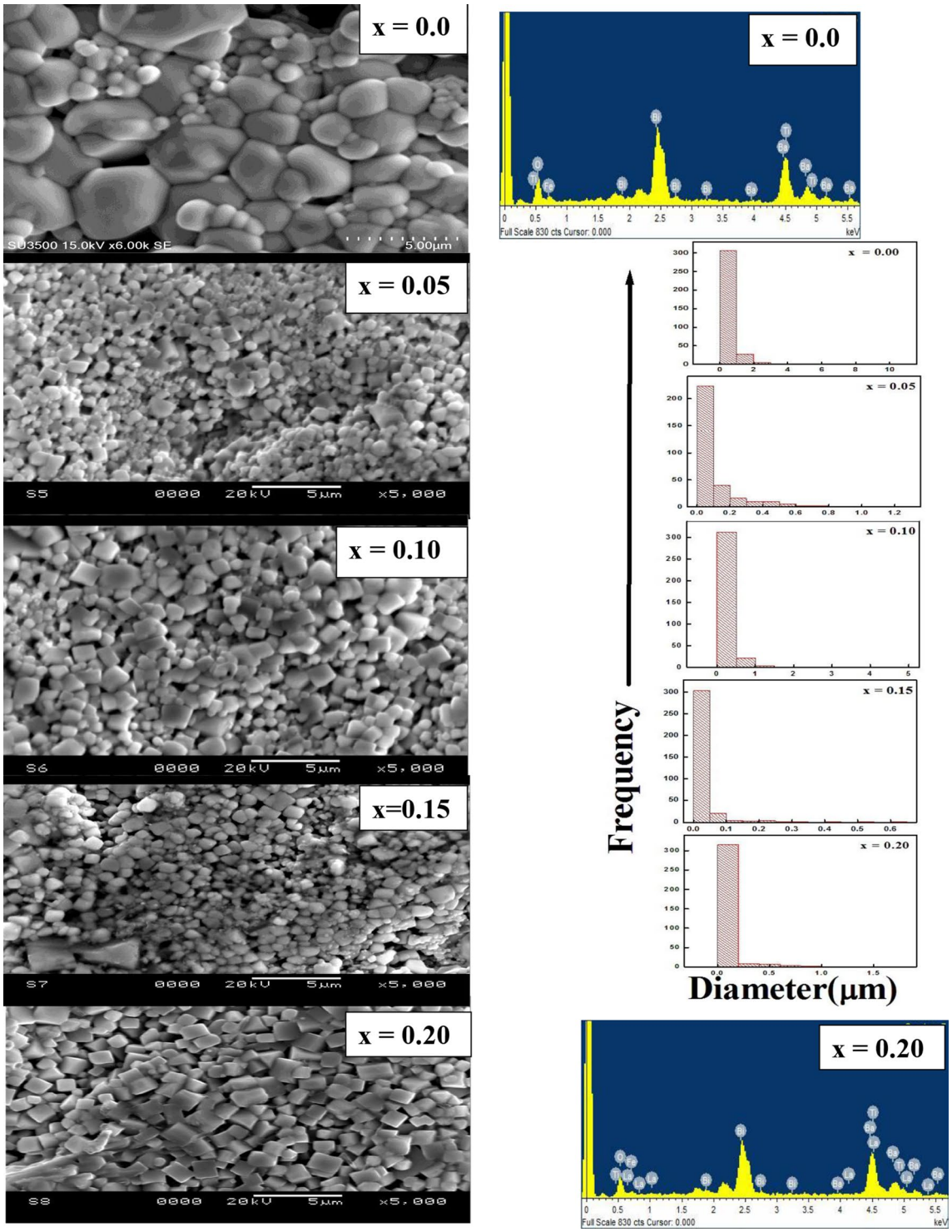

Fig. 2 SEM Micrograph of BLBFT ceramics

while the grain boundary has a generally low resistance and higher activation energy. Since, a conducting grain with an insulating grain boundary creates surface and internal barrier layer capacitor, it describes the high permittivity in the specimes [35, 36]. Though the La-modified samples show higher dielectric constant as compared to those of without *La*, however, it does not follow any strict rule of increasing the dielectric parameter with *La* concentration. This may be due to the critical statistical distribution of ions of different site. The origin of the polar region is caused by

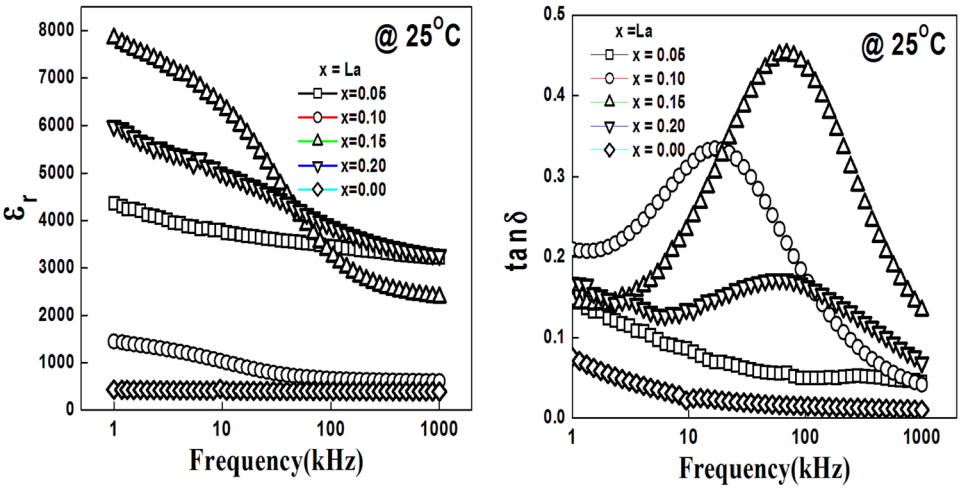

Fig. 3 Frequency dependent relative permittivity (left panel) and tangent loss(right panel)

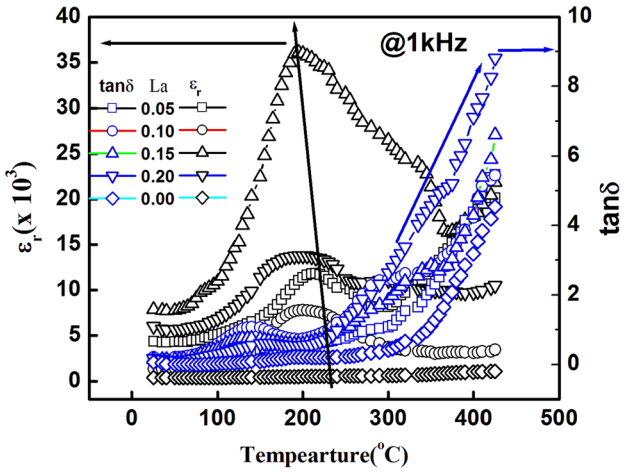

Fig. 4 temperature dependent relative permittivity and tangent loss

the structural distortion in the *La*-modified BFO–BT solid solution. Owing to the lattice matching of different sites of ions in the BFO–BT solid solution, La^{3+} ions would enter in to the Bi-site of BFO. This will lead to the formation of $(La^{3+}Bi^{3})O_6$ complexes at the Bi-site, which breaks down the long-range interactions of polar BO_6 octahedral. The increase in La^{3+} substitution in BFO–BT solid solutions disrupts the ferroelectric long-range ordering and leads to a compositional disorder, as a result, dielectric and ferroelectric characteristics of the sample changes significantly [37]

The combined compositional variant temperature-dependent relative permittivity (ε_r) and loss factor (tan δ) plots at a suitable 1 kHz frequency has been presented in Fig. 4. As evident from the figure that the all compositions exhibited typical frequency dispersion with a diffuse phase transition near the dielectric maximum temperature, while x = 0.0 composition sample dose not show any diffused phase transition. An anomaly in permittivity (shoulder around 250 °C) near dielectric maximum should be characterized as the Neel temperature (T_N), at which the magnetic ordering of $BiFeO_3$–$BaTiO_3$ is altered [38]. It is interesting to note that, for x = 0.15 and 0.20, this anomaly is significantly suppressed; that may be due to the conversion of FE to ergodic relaxor state with chemical inhomogeneity induced by BaTiO3 modification. At x = 0.20, the maximum permittivity dropped slowly by showing a flatten dielectric peak and temperature invariant dielectric permittivity over the wide range of 250–450 °C. This high flatter permittivity temperature response over a wide temperature range is surprisingly high as compared to previously reported data on Bi-based ceramics.The observed value remained higher than 5000 upto 450 °C, which is almost order of magnitude larger than the well-known Bi- and $BaTiO_3$-based dielectric materials .The temperature stable dielectric permittivity along with low dielectric losses over wide temperature range is mandatory for capacitor applications in worse atmospheric conditions. Though all sample able to maintain a stable dielectric loss over a wide range of temperature from room temperature up to 300 °C < 1; however there is a significant increase in the value of dielectric loss at higher temperatures may be due to scattering of thermally activated charge carriers and presence of some unknown defects (including oxygen vacancies) in the materials. At higher temperatures, the conductivity begins to dominate, which in turn, is responsible for rise in tagent loss. There is a possibility to reduce the oxygen vacancy concentration and stabilize Fe^{3+} valence states by the improvement of sintering technique under different atmospheres. However, the exact mechanism to improve the leakage current in BiFeO3-based systems processed by various condition is still under dispute.

As mentioned above, the substitution of *La* and *Ba* at the *Bi*-site and *Ti* at the *Fe*-site of BFO, creates some oxygen vacancies and/or lattice distortion in the materials. Therefore, the formation of these defects during high temperature

sintering ($2Fe_{Fe} + O_o \rightarrow 2Fe_{Fe} + \ddot{V}_o + 1/2O_2$) and reduction of Fe^{3+} to Fe^{2+} may be one of the main reasons for high tangent loss in BFO [2]. However, all the *La*-modified BFO–BT samples show a controlled tangent loss (< 1) suggesting the materials to be used for potential applications. The ionization of the oxygen vacancy designs to the mobile electrons in perovskite structure with *Ti*, which can be described as $V_o \leftrightarrow \dot{V}_o + e'$ and $\dot{V}_o \leftrightarrow V_o'' + e'$. These electrons may be attached to Ti^{4+} in the form of $Ti^{4+} + e' \leftrightarrow Ti^{3+}$, and at that point, it is hard to clarify whether the weakly bonded electrons are situated close to V_o or *Ti* ions [39]. In this respects, the idea of band conduction in the solid solutions might be substituted by restricted locales being encompassed by high potential wells, and consequently, can't be surpass by electrons. The creation of dipoles of the limited hopping sites resulting dielectric polarization. Consequently, the appearance of localized-charge hopping among spatially fluctuating potentials may offer accent to both the conduction and dipolar impact. The *La* substitution is more effective in controlling the volatility of *Bi* atoms, and thereby, suppresses the concentration of oxygen vacancies which helps to modify the related dielectric parameters significantly. Amid sintering process, owing to the volatile nature of *Bi*, space charges and oxygen vacancies are created [40]. In this scenario, the impact of ferroelectric domain wall pinning on the modification of physical properties of the materials may likely to be noticed. When divalent ion Ba^{2+} is substituted at trivalent ions at the *Bi*-site, substation of tetravalent Ti^{4+} ion at the trivalent *Fe*-site is required for charge balance, but oxygen vacancies is created because of valence variation of *Fe* and *Ti* ions as Fe^{3+}–Fe^{2+} and Ti^{4+}–Ti^{3+} respectively [40].

3.4 Polarization hysteresis

It is an established fact that, excellent insulation is required for complete poling of the ceramics, so that one can get more remnant polarization P_r. It is a hard task to create a dielectric breakdown under high field for the ceramics with excellent insulation. In this situation, not only more achievable polarization headings of ferroelectric domains can be modified under that field, but also favourable for domain inversion [2]. In the present ceramic samples, the electrical insulation diminishes with creation of oxygen vacancies on the substitution of Ba^{2+}. The emergence of the oxygen vacancies will cause to oxygen octahedral distortion. The pinning effect on domains reversal is caused by oxygen vacancies, which indicates that the ferroelectricity of the ceramics is enfeeble after the inclusion of the surplus di/tri valence ions.

Figure 5 exhibits the field dependence of polarization (P-E loop or hysteresis loop) of pure (x = 0.0) and *La* modified BFO–BT at room temperature with an identical working field 25 kV/cm under same condition inorder to check the hysteresis response. The appearance and nature of the loop

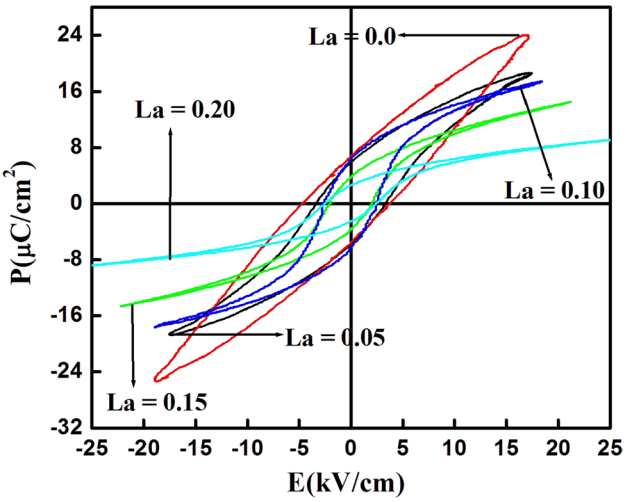

Fig. 5 P-E hysteresis loop of BLBFT at room temperature

of the BFO–BT solid solution have been modified with the addition of *La*. The value of the saturated polarization (P_s) is found to 24.1, 17.8, 16.2, 14.98, and 8.89 $\mu C/cm^2$ for the samples with x = 0, 0.05, 0.10, 0.15 and 0.20 respectively. The ferroelectric polarization of bulk bismuth ferrite is along the diagonals of the perovskite unit cell (111), pseudo-cubic (001), and hexagonal [301]. The remnant polarization (P_r) is approximately 8.1, 7.81, 7.53, 4.80 and 3.61 $\mu C/cm^2$ for x = 0, 0.05, 0.10, 0.15 and 0.20 respectively. The coercive field (E_c) is roughly about 4.78, 4.56, 2.48, 2.46 and 2.78 kV/cm for x = 0, 0.05, 0.10, 0.15 and 0.20 respectively. The polarization vector is especially adjusted to major crystallographic directions [001] and [111] for tetragonal system (with space group P4mm) and rhombohedral (with space group R3m) symmetry separately. In a tetragonal ferroelectric phase, one-sixth of the domains are already arranged along the polar axis, another one-sixth is switched by 180° and remaining two-third is turned by 90° [41].

Since $BiFeO_3$ belongs to displacive class of ferroelectrics where Bi^{3+} is a heavy ion and *6 s* orbital are more stable than *6p*. Consequently, the large radial extension of the *6 s* orbital lessens the overlapping of *6p* orbital of the both positive and negative ions which signifies the reduction of the bond strength. The energy splitting of *6 s* and *6p* orbital causes hybridization which leads to the polarization of the core *6 s* electrons. In the similar manner, the decrease and increase on either side of effective ionic radius can construct the stable bonding and octahedral distortion. Due to the repulsion experienced, the motion of the *Bi* ion towards (111) additionally causes a collective displacement of the Fe^{3+} ions, which finally helps to get high ferroelectric polarization. The polarization of core electrons and reduction of structural distortion can be achieved by an addition of Ba^{2+} and La^{3+} (with its empty *p* orbital) at the Bi^{3+}-site. It is one of the

main reasons for the decrease of P_r and P_s on increasing *La* concentration, though all the studied samples are able to maintain a well ferrolelectric behavior. The reduced rhombohedra angle infers to decrease in lattice distortion [28]. Unlike $BiFeO_3$, the displacement of the transition metal ion takes place in $BaTiO_3$. As the dislodging of cations takes place in the (001) direction, it decreases the bond separation of *Ti–O* on one side, and expands on another side.

3.5 Electrical conductivity

The ac conductivity of the materials has been evaluated using the relation: $\sigma_{ac} = \omega\varepsilon\varepsilon_0 \tan\delta$ from the dielectric data, where the parameters have their usual meanings. Similarly, the activation energy E_a, has been estimated using the relation: $\sigma_{ac} = \sigma_0 \exp(-E_a/kT)$, where k = Boltzmann constant, and σ_0 = pre-exponential factor in view of a thermally initiated process. The different slope of different frequency domains of the conductivity plot indicates the existence of multiple conduction processes with inconsistent activation energy [42]. On increasing *La* concentration, the value of σ_{ac} decreases. Figure 6 presents the frequency dependence of ac conductivity of the materials at ambient temperatures. As the conductivity is frequency dependent, it follows Jonscher's power law; $\sigma_{total} = \sigma_{dc} + A\omega^n$ [27, 43] where σ_{dc} represents the very low (dc) frequency conductivity, A is temperature dependent constant and n is temperature dependent exponent within the range of $0 \le n \le 1$. The value of A indicates the quality of polarizability, whereas the value of n suggests the level of association of mobile ions with the lattices around them [44]. The value of n decreases with rise in temperature, whereas reverse trend is observed for pre-exponential factor A. Similarly, the value of σ_{ac} increases on increasing content of *La* in the studied specimens. The origin of the frequency-dependence of conductivity lies in the relaxation process and phenomena. When a mobile charge carrier hops from its original site to a new site, it remains in a state of

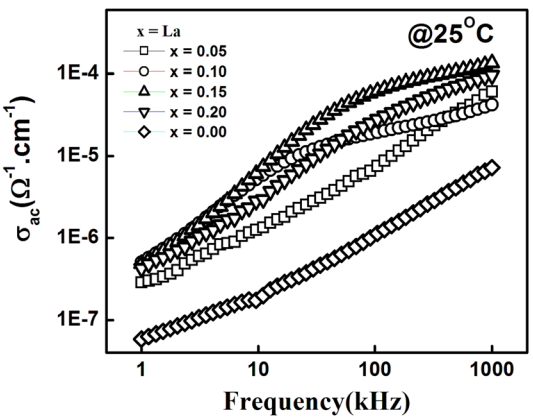

Fig. 6 Frequency dependent ac conductivity

displacement between two potential energy minima. In the meanwhile, the conductivity behaviour of the materials satisfy the universal power law; $\sigma(\omega) \propto \omega^n$ with slope change dependent on n in the low-temperature region; $n < 1$ refers to the hopping process containing a translational motion with a sudden hopping of charge carriers, whereas $n > 1$ refers to the localized hopping without the species leaving the neighbourhood undisturbed [6, 45, 46]. The frequency at which change slope takes place, is known as hopping frequency of the polarons (ω_p), and also is temperature dependent. The high-frequency dispersion is ascribed to the *ac* conductivity whereas the frequency independent plateau region repents *dc* conductivity. Thus, studied materials satisfy universal power law.

3.6 Magnetic properties

The magnetic properties of $BIFeO_3$ and its derivatives can be modified by the suitable modification of ions in its different site. A number of studies show that by the introduction of magnetic or non magnetic compounds such as BaTiO3, $La_{0.67}Sr_{0.33}MnO_3$, $GdCrO_3$, $Pb(Zr_{0.52}Ti_{0.48})O_3$ etc can enhance/stabilize the magnetic properties of $BiFeO_3$ [28]. Since *d* orbital of Fe^{3+}, satisfy the condition of both half filled and localized (t^3_{2g}, e^2_g) criteria, the degeneracy increases where every orbital having an integral number of *d* electrons per shell (n_l). Therefore, the movement of electron occurs only when $n_l = 1$. When $n_l = 0$ or 2, it causes to the vacant and/or fully filled orbital, especially under the said conditions, Pauli exclusion principle permits the convey of electron to the adjacent ion only in the anti-parallel direction which confirms a *G*-type anti-ferromagnetic ordering of $BiFeO_3$ (between two adjacent *Fe* ions). The ferromagnetism behaviour found in present studied systems might be due to the spin canting. In the distorted cubic (rhombohedral) domain, the *Fe–O–Fe* spins are no longer collinear, and thus a little spin canting might happen, leading to a ferromagnetic state in present system [28].

Figure 7 shows magnetic field (H) dependence of magnetization (M) (i.e., M-H hysteresis loop) of $(Bi_{0.5-x}La_xBa_{0.5})(Fe_{0.5}Ti_{0.5})O_3$ with x = 0.0, 0.05, 0.10, 0.15, 0.20 recorded at room temperature. For the samples with x = 0.0–0.10, the BFO–BT solid solutions exhibit a typical weak ferromagnetism. On increasing *La* content of the solid solution, both saturated (M_s) and remnant magnetization (M_r) decrease (Fig. 7). As the content of BT is fixed, the variation of *La* content in $BiFeO_3$-$BaTiO_3$ may be responsible for change from weak ferromagnetic to an anti-ferromagnetic state with a considerable change in magnetic moment. Again, both structural distortion and statistical distribution of Fe^{3+} and Ti^{4+} on the octahedral sites lead to the amplification in ferromagnetism of BFO–BT solid solutions [47]. The incorporation of La^{3+} and Ba^{2+} into Bi^{3+} sites and Ti^{4+} into Fe^{3+}

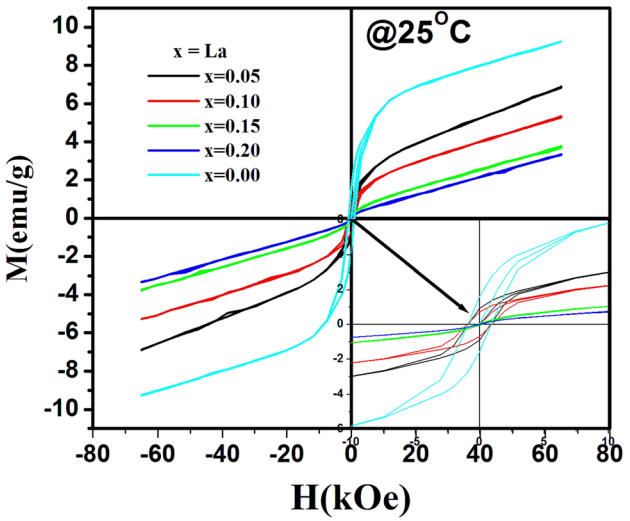

Fig. 7 Fig. 4. M-H hysteresis BLBFT Solid solutions

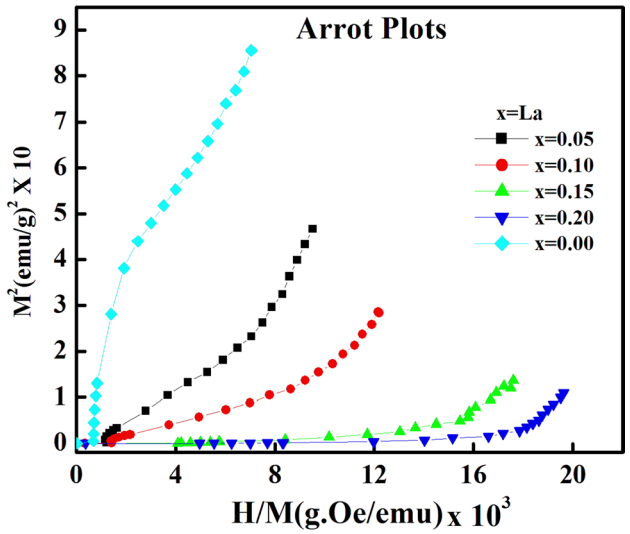

Fig. 8 Arrot plot of BLBFT Solid solutions

sites hold up canted spin settlement of unpaired electrons of the Fe^{3+} ions. Because of the introduction of $BaTiO_3$ into $BiFeO_3$, the magnetic spiral symmetry is repressed owing to the Ti^{4+} into Fe^{3+} site which separates *Fe–O–Fe* super-exchange interaction and also promote the electric polarization by altering the symmetry of sample [48].The addition of La will results an increase in the macroscopic magnetization of $BiFeO_3$ in BFO–BT solid solutions, which was attributed to the formation of Fe^{2+} with a suppressed inhomogeneous magnetic spin structure and an increasing canting angle [28].

For checking the change of magnetic nature of the solid solutions, Arrot plots (M^2 *vs.* *M*/*H* curves) were constructed by using the magnetization curves of the BFO–BT solid solutions and presented in Fig. 8. It is evident from the plots that, since BT concentration remains fixed, only the variation in the *La* concentration, and hence the Arrot plots in high magnetic fields are parallel to each other for x = 0 to x = 0.10 revealing the similar magnetic behaviours in this composition range where as for x = 0.15 and 0.20 the Arrot plots are no longer parallel to the rest two composition, revealing the different magnetic behaviour [20].

Above mentioned results exhibit not only the balancing of crystal structure, but also non uniformity in spin cycloid structure by *La* substitution, and also intensify the multiferroic properties of $BiFeO_3$–$BaTiO_3$ solid solution.

4 Conclusion

A series of *La*-modified BFO-BT solution has been prepared via a conventional but standard economical synthesis technique with pure phase in the R3c crystallographic symmetry. No secondary phase is observed in the *La*- modified solid solution suggesting that pure phase can be obtained with the suitable modification by rare earth and it was confirmed by the Reitveld refinement. The high value of dielectric permittivity suggests the material for possible application in capacitive energy storage devices. The *Fe–O–Fe* interaction concludes anti-ferromagnetic ordering, because of canting of the spins in the distorted perovskite, compositional dependent of ferromagnetic as well as anti-ferromagnetic characteristics. The extracted and composition dependent ferroelectric and ferromagnetic properties suggest the material to be a potential candidate for multifunctional devices. With increasing *La* concentration, the structure becomes simpler and anti-ferromagnetic sets in as BFO.

Acknowledgements Author (CB) is gratefully acknowledged the grant received from SERB, DST, Govt. of India (PDF/2016/001078 dated 26th July.2016) to carry out the research work and CRF,IIT Kharagpur for SEM and SQUID facility.

References

1. M. Lorenz, D. Hirsch, C. Patzig, T. Höche, S. Hohenberger, H. Hochmuth, V. Lazenka, K. Temst, M. Grundmann, ACS Appl. Mater. Interfaces **9**, 18956–18965 (2017)
2. Y. Guo, P. Xiao, R. Wen, Y. Wan, Q. Zheng, D. Shi, K. Ho Lam, M. Liu, D. Lin, J. Mater. Chem. C **3**, 5811 (2015)
3. C.S. Tu, R.R. Chien, T.-H. Wang, J. Anthoninappen, Y.-T. Peng, J. Appl. Phys. **113**, 17D908 (2013)
4. S. Kim, G.P. Khanal, H.-W. Nam, I. Fujii, S. Ueno, C. Moriyoshi, Y. Kuroiwa, S. Wada, J. Appl. Phys. **122**, 164105 (2017)
5. W. Gao, J. Lv, X. Lou, J. Am. Ceram. Soc. **101**, 3383–3392 (2018)
6. S. Jangra, S. Sanghi, A. Agarwal, M. Rangi, K. Kaswan, Ceram. Int., **44**, 7683–7693(2018)
7. Y. Wei, X. Wang, J. Zhu, X. Wang, J. Jia, J. Am. Ceram. Soc. **96**, 3163 (2013)
8. J. Zhuang, J. Zhao, L.-W. Su, H. Wu, A.A. Bokov, W. Ren, Z.-G. Ye, J. Mater. Chem. C **3**, 12450–12456 (2015)

9. S. Murakami, N. Thafeem, A. Faheem Ahmed, D. Wang, A. Feteira, D.C. Sinclair, I.M. Reaney, J. Eur. Ceram. Soc. **38**, 4220–4231 (2018)
10. W. Dong, Y.P. Guo, B. Guo, H.Y. Liu, H. Li, H.Z. Liu, Mater. Lett. **91**, 359 (2013)
11. X.J. Xi, S.Y. Wang, W.F. Liu, H.J. Wang, F. Guo, X. Wang, J. Gao, D.J. Li, J. Magn. Magn. Mater. **355**, 259 (2014)
12. Z. Jia, X. Wu, M. Zhang, J.J. Liou, Ferroelectrics **504**, 172–179 (2016)
13. A. Ahlawat, S. Satapathy, R.J. Choudhary, M.K. Singh, P.K. Gupta, Mater. Lett. **181**, 123–126 (2016)
14. S.N. Das, S.K. Pradhan, S. Bhuyan, et.al., J. Mater. Sci.: Mater. Electron. **28**, 18913 (2017)
15. T. Zheng, J. Wu, Quenched bismuth ferrite-barium titanate lead-free piezoelectric ceramics. J. Alloys Compd. **676**, 505–512 (2016)
16. S. Unruan, M. Unruan, T. Monnar, S. Priya, R. Yimnirun, J. Am. Ceram. Soc. **98**, 3291 (2015)
17. H.L. Zhang, W. Jo, K. Wang, K.G. Webber, Ceram. Int. **40**, 4759 (2014)
18. T.H. Wang, C.S. Tu, Y. Ding, T.C. Lin, C.S. Ku, W.C. Yang, H.H. Yu, K.T. Wu, Y.D. Yao, H.Y. Lee, Curr. Appl. Phys. **11**, S240–S243 (2011)
19. T.J. Park, G.C. Papaefthymiou, A.J. Viescas, Y. Lee, H. Zhou, S.S. Wong, Phys. Rev. B **82**, 024431 (2010)
20. R.A.M. Gotardo, D.S.F. Viana, M. Olzon-Dionysio, S.D. Souza, D. Garcia, J.A. Eiras, M.F.S. Alves, L.F. Cotica, I.A. Santos, A.A. Coelho, J. Appl. Phys. **112**, 104112 (2012)
21. Y.T. Peng, S.H. Chiou, C.H. Hsiao, C. Ouyang, C. Tu, Sci. Rep. **7**, 45164 (2017)
22. T. Zheng, J. Wu, J. Mater. Chem. C **3**, 3684 (2015)
23. S. Sharma, V. Singh, A. Anshul, J.M. Siqueiros, R.K. Dwivedi, J. Appl. Phys. **123**(20), 204102 (2018)
24. C. Behera, R.N.P. Choudhary, P.R. Das, J. Mater. Sci.: Mater. Electron. **25**, 2086 (2014)
25. M. Shariq, D. Kaur, V.S. Chandel, Chin. J. Phys. **55**, 2192–2198 (2017)
26. M.H. Lee, D.J. Kim, J.S. Park, M.-H. Kim, T.K. Song, S. Kumar, W.J. Kim, D. Do, I. Hwang, B.H. Park, K.S. Choi, Curr. Appl. Phys. **16**, 1449–1452 (2016)
27. X. Qi, M. Zhang, X. Zhang, Y. Gu, H. Zhu, W. Yanga, Y. Lia, RSC Adv. **7**, 51801 (2017)
28. J. Wu, Z. Fan, D. Xiao, J. Zhu, J. Wang, Prog. Mater. Sci. **84**, 335–402 (2016)
29. T.H. Wang, C.S. Tu, H.Y. Chen, Y. Ding, T.C. Lin, Y.D. Yao, V.H. Schmidt, K.T. Wu, J. Appl. Phys. **109**, 044101 (2011)
30. E. Wu, POWD, School of Physical Sciences, Flinders University South Bedford Park, SA 5042 Australia
31. M.W. Lufaso, T.A. Vanderach, M. Pazos, I. Levin, R.S. Roth, J.C. Nio, V. Provenzano, P.K. Schenck, J. Solid State Chem. **179**, 3900 (2006)
32. J.R. Cheng, L.E. Cross, J. Appl. Phys. **94**, 5188 (2003)
33. T. Leist, K.G. Webber, W. Jo, T. Granzow, E. Aulbach, J. Suffner, J. Rödel, J. Appl. Phys. **109**, 054109 (2011)
34. L. Zivkovie, V. Paunovie, M. Milijkovie, M.M. Ristic, Mat. Sci. Forum **518**, 229 (2006)
35. C. Behera, R.N.P. Choudhary, P.R. Das, Struct. Mater. Res. Exp. **5**, 056301 (2018)
36. D.C. Sinclair, T.B. Adams, F.D. Morrison, A.R. West, Appl. Phys. Lett. **80**, 2153 (2002)
37. V.I. Gibalov, G.J. Pietsch, Plasma Sources Sci. Technol. **21**, 024010 (2012)
38. R. Ahmed Malik, A. Zaman, A. Hussain, A. Maqbool, T.K. Song, W.J. Kim, Y.S. Sung, M.H. Kim, J. Eur. Ceram. Soc. **38**, 2259–2263 (2018)
39. Z. Cen, C. Zhou, H. Yang, Q. Zhou, W. Li, C. Yan, L. Cao, J. Song, L. Peng, J. Am. Ceram. Soc. **96**, 2252 (2013)
40. A. Chen, Y. Zhi, L.E. Cross, Phys. Rev. B **62**, 228 (2000)
41. J.E. Garcia, V. Gomis, R. Perez, A. Albareda, J.A. Eiran, Appl. Phys. Lett. **91**, 0429021 (2007)
42. Z. Dai, Y. Akishige, J. Phys. D **43**, 445403 (2010)
43. L. Bellaiche, A. Garcı´a, D. Vanderbilt, Phys. Rev. B **64**, 060103 (2001)
44. K.S. Kumar, C. Venkateswar, D. Kannan, B. Tiwari, M.S.R. Rao, J. Phys. D **45**, 415302 (2012)
45. S. Shankar, Brijmohan, S. Kumar, O.P. Thakur, A.K. Ghosh, Phys. Lett. A **381**, 379–386 (2017)
46. S.K. Singh Patel, J.H. Lee, M.-K. Kim, B. Bhoi, S.-K. Kim, J. Mater. Chem. C **6**(3), 526 (2018)
47. S. Chandarak, M. Unruan, T. Sareein, A. Ngamjarurojana, S. Maensiri, P. Laoratanakul, S. Ananta, R. Yimnirun, J. Magn. **14**, 120 (2009)
48. R. Cohen, Nature **358**, 136 (1992)